Chapter 6
Details of Fabrication Techniques of Various Lotus Metals and Alloys, Lotus Intermetallic Compounds, Lotus Semiconductors, and Lotus Ceramics

Abstract Case studies are shown by different atmospheric gases and by different materials such as intermetallic compounds, semiconductors, ceramics, and magnesium and iron alloys.

Keywords Alumina • Aluminum • Ceramics • Czochralski technique • Intermetallic compounds • Iron • Silicon • Solid-state diffusion

6.1 Fabrication of Lotus Iron by Nitrogen

So far hydrogen has widely been used as a dissolving gas to fabricate several kinds of porous metals such as lotus metals. However, since the hydrogen gas is inflammable and explosive, its use is not convenient from the industrial point of view. Use of other gases except hydrogen would be desirable. It is well known that nitrogen is an important alloying element widely used to improve corrosion resistance and mechanical properties of steels [1]. Hyun and Nakajima noticed that the temperature dependence of nitrogen solubility in solid and liquid of iron is similar to that of hydrogen [2], which exhibits large nitrogen solubility difference between solid and liquid iron at the melting temperature [3]. Moreover, it is noticed that an invariant reaction of "gas-evolution crystallization reaction" [4] takes place in the Fe–N system, in which the iron melt dissolving nitrogen is solidified to transform into the primary solid solution and nitrogen gas phase. Utilizing the nitrogen solubility difference between liquid and solid, it is possible to fabricate porous iron using safe nitrogen gas instead of hydrogen gas. This new type of porous iron is promising for commercial application.

Figure 6.1 shows the typical optical micrographs of the cross section at the bottom part of the ingot. The overall porosity was measured as functions of the partial pressures of nitrogen and argon. The porosity was found to be affected by the nitrogen and argon pressures, which is similar to the system of hydrogen–argon gas. At a given nitrogen pressure, the porosity decreases with increasing argon

H. Nakajima, *Porous Metals with Directional Pores*,
DOI 10.1007/978-4-431-54017-5_6, © Springer Japan 2013

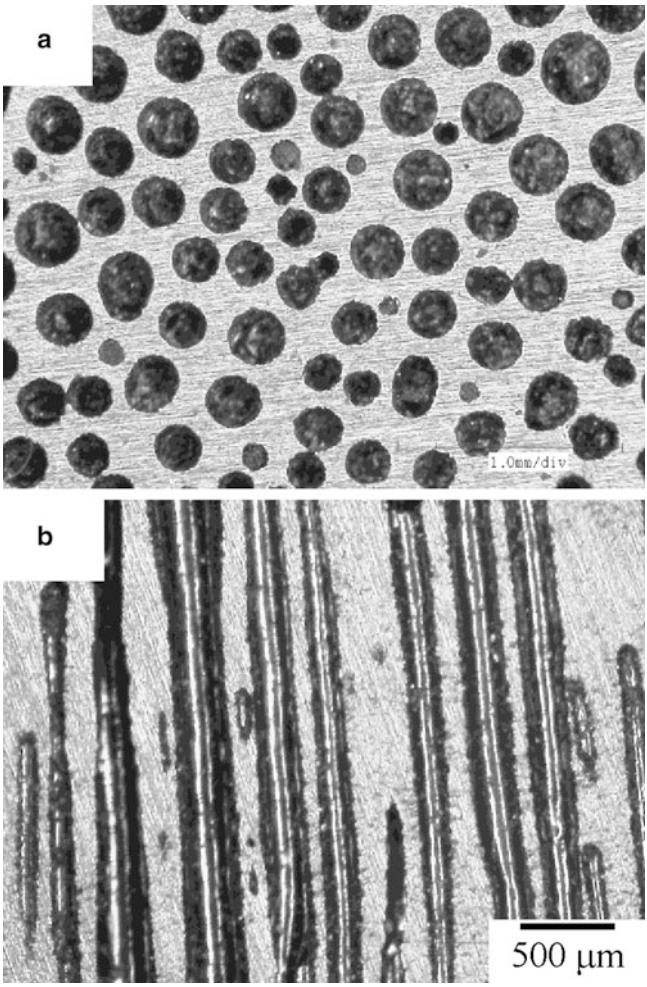

Fig. 6.1 Optical micrographs of cross sections of lotus iron with 37.7 % porosity. The total pressure 1.5 MPa with the partial pressure of nitrogen of 1.0 MPa and the partial pressure of argon of 0.5 MPa. (**a**) Cross section perpendicular to the pore axis and (**b**) cross section parallel to the pore axis (Reprinted with permission from [2]. © 2002 Japan Institute of Metals)

pressure as shown in Fig. 6.2a. At a given argon pressure, the porosity increases with increasing nitrogen pressure as shown in Fig. 6.2b.

The solubility of nitrogen in iron is proportional to the square root of the nitrogen gas pressure, $\sqrt{P_{N_2}}$, according to Sieverts' law:

$$\left.\begin{aligned} C_N^L &= K^L\sqrt{P_{N_2}} \\ C_N^\delta &= K^\delta\sqrt{P_{N_2}} \end{aligned}\right\}, \tag{6.1}$$

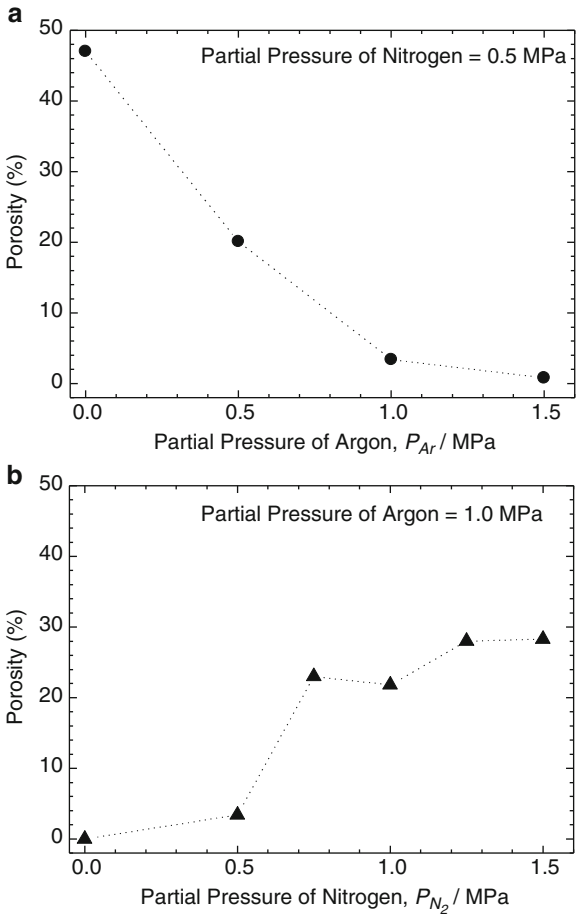

Fig. 6.2 Dependence of porosity in lotus iron on (**a**) the partial pressure of argon at nitrogen pressure of 0.5 MPa and (**b**) the partial pressure of nitrogen at argon pressure of 1.0 MPa (Reprinted with permission from [2]. © 2002 Japan Institute of Metals)

where $C_{\mathrm{N}}^{\mathrm{L}}$ and C_{N}^{δ} are the nitrogen concentration in the liquid and the δ-iron, respectively, and K^{L} and K^{δ} are equilibrium constants given by

$$K = \exp\left(-\frac{\Delta G}{RT}\right) = \exp\left(\frac{\Delta S}{R} - \frac{\Delta H}{RT}\right), \tag{6.2}$$

where ΔG is the Gibbs energy change for the solution of nitrogen, T is an absolute temperature, R is the gas constant, and ΔH and ΔS are the standard enthalpy and entropy of solution of nitrogen, respectively. The solubility of nitrogen in the different iron phases is usually evaluated from the slope of the decomposition pressure on logarithmic scale against $1/T$ [5]. The solubility of nitrogen in the molten iron is much higher than that of δ-iron as shown in Fig. 6.3. Therefore, nitrogen in the molten iron is rejected at the solid–liquid interface during solidification and the pores nucleate and grow unidirectionally. Considering the mixture

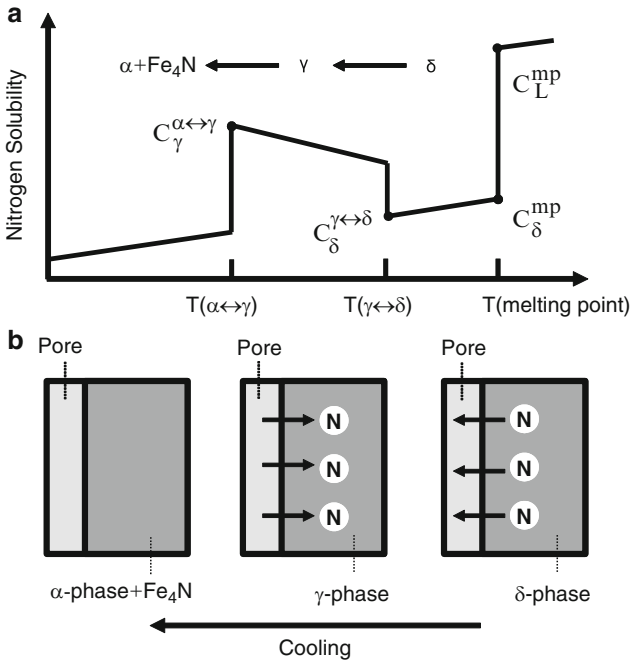

Fig. 6.3 (**a**) Temperature dependence of nitrogen solubility in iron and (**b**) schematic of nitrogen movement during cooling after solidification in lotus iron fabricated with nitrogen gas (Reprinted with permission from [2]. © 2002 Japan Institute of Metals)

gas of nitrogen and argon, although the solubility of nitrogen in liquid is determined by the partial pressure of nitrogen, the nitrogen solubility near the pores is related with the internal gas pressure P_i for satisfying with the equilibrium between solid phase around the pores and gas phase in the pores. Therefore, Eq. (6.1) can be written as

$$C_N^\delta = K^\delta \sqrt{P_i}. \tag{6.3}$$

From this equation, it can be seen that the solubility of nitrogen in solid is related with total pressure of nitrogen and argon. With increasing partial pressure of argon at a given total pressure, the nitrogen solubility in liquid decreases but the nitrogen solubility in solid is almost constant.

Figure 6.4 shows the nitrogen concentration in the matrix of lotus iron as a function of the partial pressure of nitrogen when the total gas pressure of nitrogen and argon is kept constant at 2.0 MPa. It was found that the measured nitrogen concentration is in the range from 0.06 to 0.135 mass%. According to the solubility curve of nitrogen in iron [5], the nitrogen solubility in γ-iron decreases with increasing temperature and the maximum solubility is 0.135 mass% at the lowest

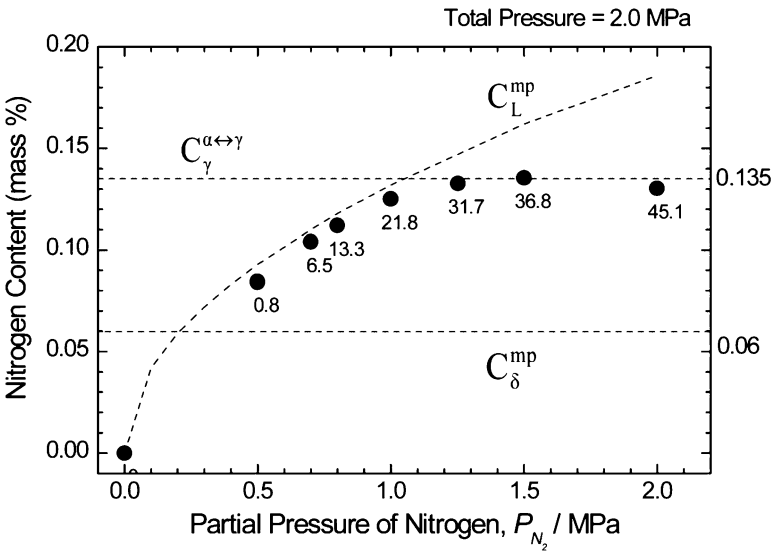

Fig. 6.4 Nitrogen concentration in the matrix of lotus iron versus the partial pressure of nitrogen gas under constant total pressure of 2.0 MPa (Reprinted with permission from [2]. © 2002 Japan Institute of Metals)

temperature of the γ-phase. On the other hand, in δ-iron, the nitrogen solubility increases with increasing temperature and the maximum solubility is calculated as 0.06 mass% at the temperature just below the melting point of iron. Thus, it is reasonable that the measured nitrogen concentration range as shown in Fig. 6.4 is in between these two limits of the solubility. The reason why the measured nitrogen concentration is much higher than the nitrogen solubility in δ-iron can be explained as follows. As shown in Fig. 6.3 when the molten iron is solidified in the pressurized mixture gas of nitrogen and argon, the pores are formed by the evolution of nitrogen insoluble in the solid iron. In the subsequent cooling process in the solid, the nitrogen solubility in δ-iron gradually decreases with decreasing temperature. Then, the insoluble nitrogen atoms $(C_\delta^{mp} - C_\delta^{\gamma\leftrightarrow\delta})$ diffuse into the pores from δ-iron matrix. However, in further cooling process in γ-iron, the nitrogen solubility abruptly increases at the $\delta \rightarrow \gamma$ phase transformation temperature and continues to increase with decreasing temperature until the $\gamma \rightarrow \alpha$ phase transformation temperature is reached. In this process the nitrogen gas in the pores is dissolved into the γ-iron. Finally, two phases of α(ferrite) phase and Fe_4N compound are formed on the phase transformation from γ-phase to α-phase.

Figure 6.5 shows the microstructure of the specimen containing 0.137 mass% nitrogen in the matrix of quenched porous iron which was fabricated in the mixture gas of $P_{N_2} = 1.25$ MPa and $P_{Ar} = 0.75$ MPa. The proeutectoid ferrite was observed on the grain boundaries and also inside the grains in the as-cast porous iron.

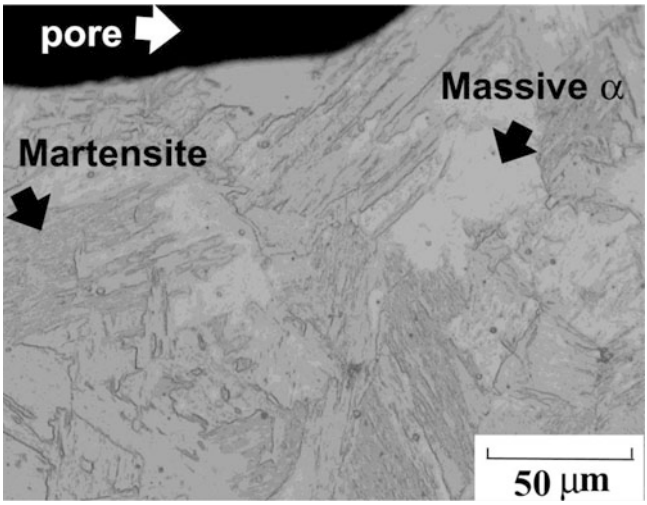

Fig. 6.5 Optical micrograph of as-quenched lotus iron containing 0.137 mass% nitrogen in the matrix fabricated in the mixture gases of nitrogen 1.25 MPa and argon 0.75 MPa (Reprinted with permission from [2]. © 2002 Japan Institute of Metals)

6.2 Fabrication of Lotus Silver by Oxygen

In most combinations of the metals and gas such as hydrogen or nitrogen, the gas solubility in both of liquid and solid phases tends to decrease with decreasing temperature. However, a unique tendency is observed in the silver–oxygen system; the oxygen solubility in liquid silver increases with decreasing temperature [6]. It is interesting to know the effect of such an inverse temperature dependence of solubility on the pore formation and growth during the unidirectional solidification. The lotus-type porous silver was produced by unidirectional solidification through the mold casting technique and the Czochralski technique under pressurized oxygen [7]. Figure 6.6 shows a schematic picture of the apparatus for the Czochralski technique consisting of a melting part and a transfer mechanism of the rod in a high-pressure chamber. First, silver in an alumina crucible was melted by an induction heating in a mixture gas of oxygen and argon under a given pressure. A silver rod set upward was moved down to the surface of the melt, and then the rod was moved upward at the rate of 1.6 mm min^{-1}. The dimensions of the resulting silver ingot were about 15 mm in diameter and 100 mm in height.

The shape of pores in porous silver is different from those in other lotus copper and iron. Figure 6.7 shows an example of optical microscopic observation of the structure of lotus-type porous silver fabricated by the mold casting technique, indicating the cross section parallel and perpendicular to the solidification direction. In the cross section parallel to the solidification direction, although characteristic

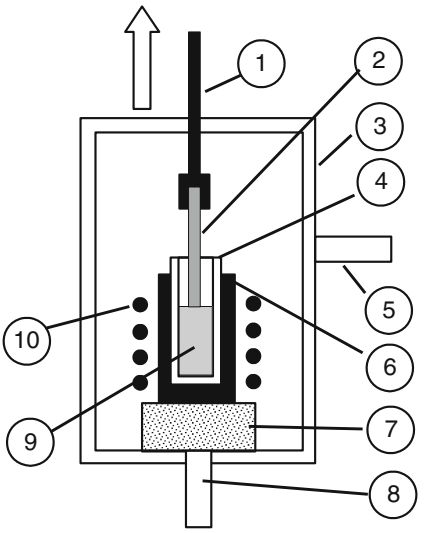

Fig. 6.6 Schematic drawing of the apparatus of Czochralski method for fabricating lotus silver (Reprinted with permission from [7]. © 2005 Japan Institute of Metals)

cylindrical pores were observed to extend to the solidification direction, their shapes are not straight and their diameters are not constant in the direction. Similarly the pore shape is distorted, the distribution density of pores is not homogeneous, and furthermore, the pore size distribution is broad in the cross section of the perpendicular direction compared with other lotus metals. Such particular features to porous silver are discussed on the basis of the binary equilibrium phase diagram. A schematic drawing of the binary equilibrium phase diagram for silver–oxygen system is illustrated in Fig. 6.8, where T_m and T_n mean the holding temperatures of silver melt in oxygen (1,573 K) and the gas-evolution crystallization reaction temperature, respectively. On the assumption that the solidification progresses in equilibrium state, oxygen concentration of the liquid silver increases from A to B with decreasing temperature. Subsequently at T_n the reaction of $L \rightarrow (S) + G$ occurs. In this case the solid phase appears below T_n, expecting that the pore shape would be similar to that of other lotus metals. However, the experimental results are not the case. Thus, it is reasonable to consider that the solidification progresses in nonequilibrium state by rapid cooling without

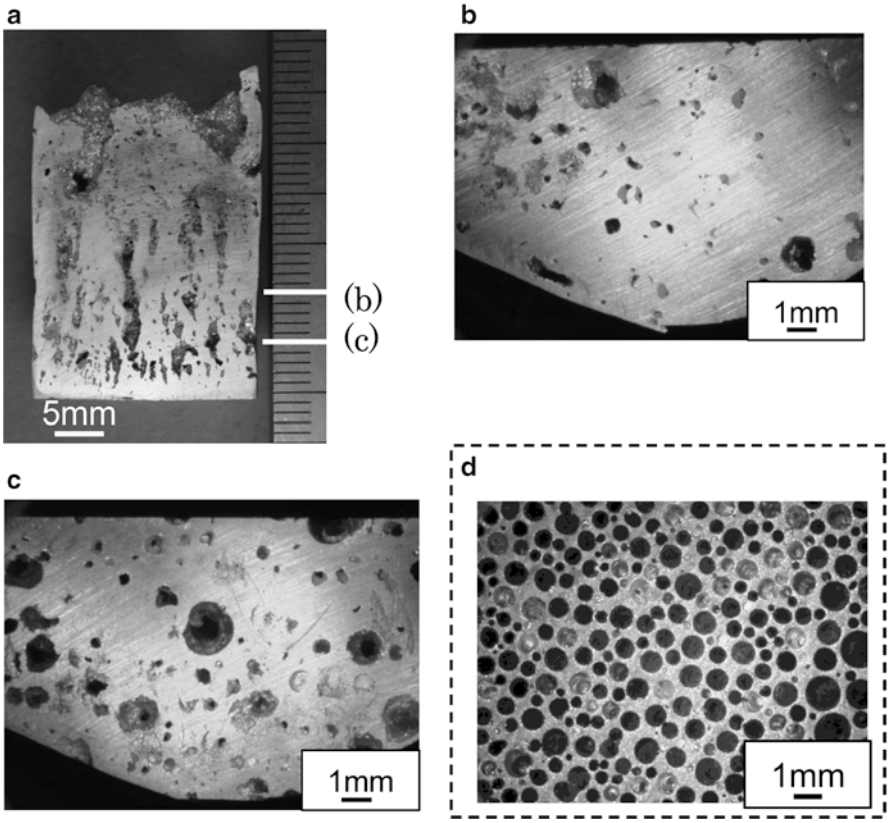

Fig. 6.7 Cross sections of lotus silver fabricated by the mold casting technique under 0.05 MPa of oxygen and 0.15 MPa of argon. (**a**) Parallel to the solidification direction and (*b*, *c*) perpendicular to the solidification direction at the distance (**b**) 10 mm and (**c**) 5 mm from the copper chiller (the bottom). (**d**) Cross section perpendicular to the solidification direction of lotus copper (Reprinted with permission from [7]. © 2005 Japan Institute of Metals)

oxygen supply from the gas phase to the liquid phase and the oxygen concentration of the liquid phase is constant from A to C. In this case unlike other lotus metals, the solidification progresses through $L + (S)$ phase: the solid phase coexists with the liquid phase. This can prevent the growth of cylindrical pores similar to the case of lotus magnesium alloys [8]. Thus, the solidification in the $L + (S)$ phase could be a part of reason for the distorted pore shape.

Figure 6.9 shows the cross section parallel and perpendicular to the solidification direction of the specimen fabricated by the Czochralski technique. The distribution density of pores fabricated by the Czochralski technique is more homogeneous than that by the mold casting technique. In the Czochralski technique, the liquid phase continuously contacts the gas phase during the solidification. Thus, it is expected that oxygen can easily be supplied from gas phase to the liquid–solid interface and

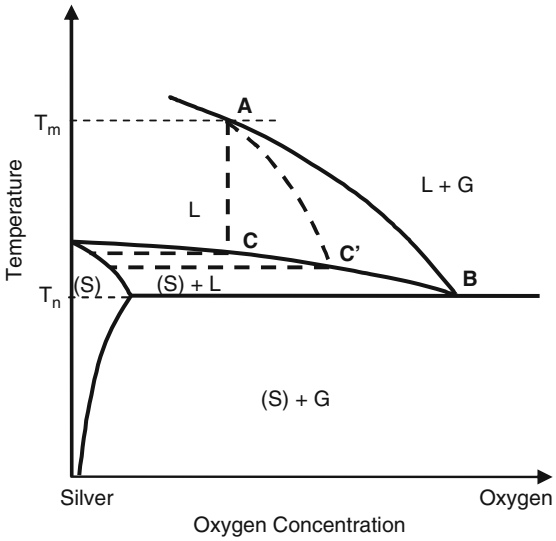

Fig. 6.8 Silver-rich side of binary equilibrium phase diagram for silver–oxygen system (Reprinted with permission from [7]. © 2005 Japan Institute of Metals)

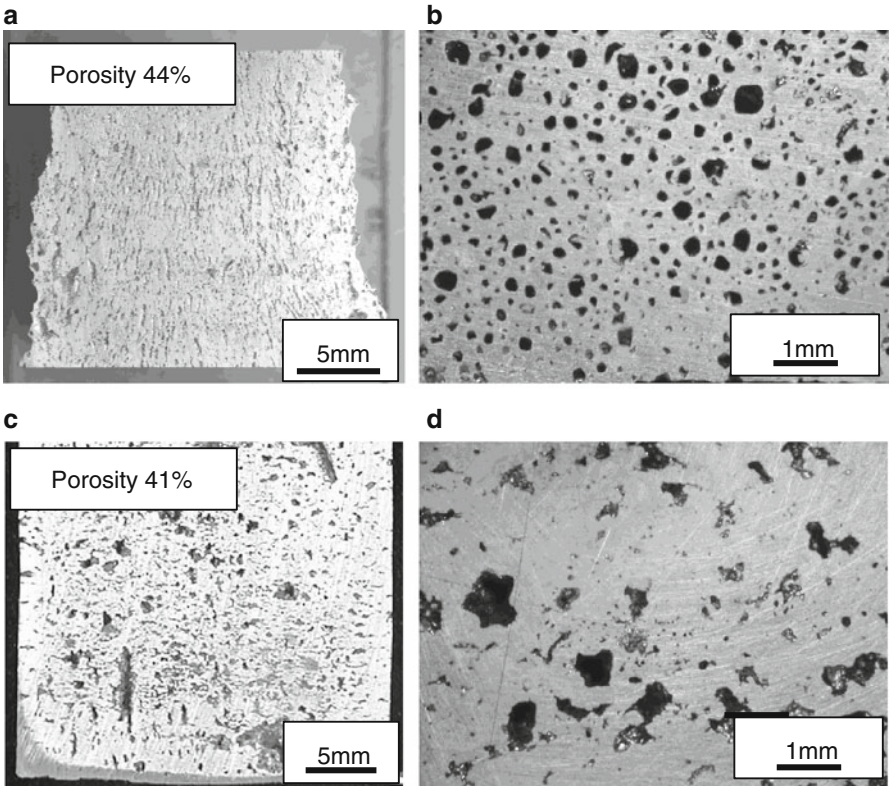

Fig. 6.9 Cross sections of lotus silver by the Czochralski method. (**a**) Parallel to the solidification direction and (**b**) perpendicular to the solidification direction. Cross sections of the lotus silver fabricated by the mold casting technique: (**c**) parallel to the solidification direction and (**d**) perpendicular to the solidification direction. The atmosphere was a mixture of 0.55 MPa of oxygen and 0.55 MPa of argon (Reprinted with permission from [7]. © 2005 Japan Institute of Metals)

then the porosity also must increase. The distribution of the pore size σ and the circularity R at the cross section perpendicular to the solidification direction are calculated as

$$\sigma = \sigma_s / d_a$$
$$R = 4\pi \times A / L^2, \tag{6.4}$$

where σ_s, d_a, A, and L are the standard deviation of pore sizes, the average pore diameter, the area of pores, and the circumference length of the pores, respectively. It turned out that the distribution of pore size σ decreases and the circularity R increases in the lotus silver made by the Czochralski technique compared with the ingot obtained by the mold casting method. These results support the assumption that the oxygen gas in the pores formed at the liquid–solid interface redissolves to the molten silver with insufficient oxygen concentration in the fabrication by the unidirectional solidification method.

6.3 Fabrication of Lotus Intermetallic Compounds

Intermetallic compounds exhibit superior properties of high-temperature strength, oxidation resistance, and anti-corrosion and are expected to be used as high-temperature structural materials and functional materials. If elongated pores aligned in one direction can be evolved in the intermetallic compounds, various applications such as lightweight high-temperature structural materials, high-temperature catalyst, and high-temperature filters can be expected. In particular, aluminide intermetallic compounds have attracted much attention for lightweight high-temperature materials [9–11]. Recently Hyun et al. [12] fabricated lotus-type porous intermetallic compounds of Ni_3Al and TiNi for the first time.

Figure 6.10 shows optical micrographs of the cross-sectional views of lotus-type porous NiAl compounds perpendicular to the solidification direction fabricated by the continuous zone melting technique. The fabrication was carried out at 2.5 MPa hydrogen and with the transfer velocity of 330 μm s^{-1}. The pores in lotus Ni-15%Al alloy are round, while those in lotus Ni-28%Al and Ni-31%Al alloys are in distorted morphology. The solidification structures in longitudinal cross section parallel to the solidification direction are shown in Fig. 6.11. The dendritic structure is observed in the Ni-28%Al alloy. When the pores nucleated in apertures of the dendrite grow, the pores may touch to the dendritic arms and cannot grow straight, which result in distorted pore morphology. On the other hand, in Ni-15%Al alloy no dendrite structure is observed so that round-shaped pores observed in the section perpendicular to the solidification direction grow straight in the solidification direction. This is attributed to the narrow two phases' region of mixture of liquid and solid and to the suppressive growth of the dendritic arms.

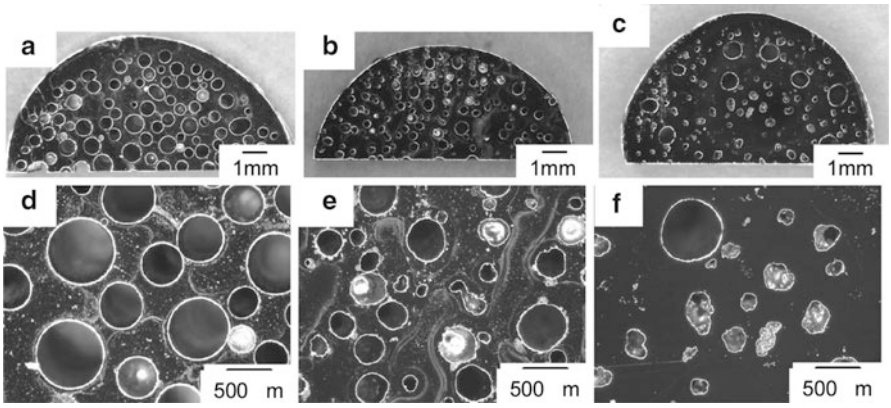

Fig. 6.10 Optical micrographs of lotus (**a**, **d**) Ni-15%Al, (**b**, **e**) Ni-28%Al, and (**c**, **f**) Ni-31%Al intermetallic compounds in the cross sections perpendicular to the solidification direction fabricated by continuous zone melting technique in 2.5 MPa hydrogen atmosphere (Reprinted with permission from [12]. © 2004 Japan Institute of Metals)

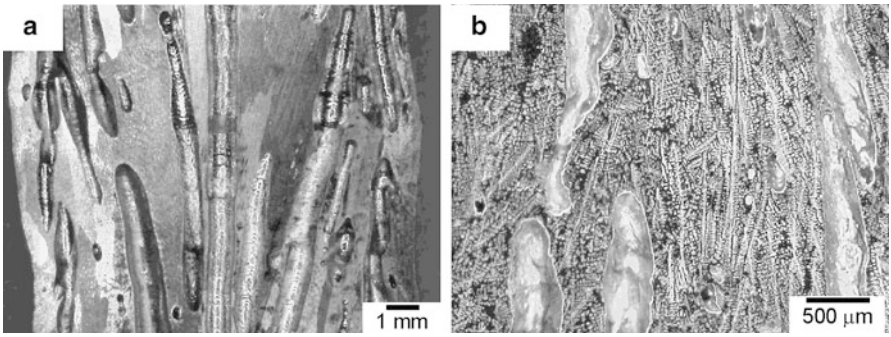

Fig. 6.11 Optical micrographs of lotus (**a**) Ni-15%Al and (**b**) Ni-28%Al intermetallic compounds in section parallel to the solidification direction (Reprinted with permission from [12]. © 2004 Japan Institute of Metals)

The porosity decreases from 40 to 18 % with increasing Al content from 15 to 31 %. The porosity is closely related with and proportional to the hydrogen concentration rejected at the liquid–solid interface. According to Lange and Schenck [13], the addition of aluminum to nickel suppresses the hydrogen solubility in the liquid. For example, the hydrogen solubility in Ni-25%Al alloy at 1,773 K under 0.1 MPa hydrogen pressure is about 50 % smaller than that in pure nickel. Therefore, the decrease in porosity may be due to the decrease in hydrogen content available to the pore evolution. The average pore diameter decreases with increasing Al content, which is also attributed to the same reasoning.

6.4 Fabrication of Lotus Silicon

Porous silicon with nano-order sized pores was fabricated by electrolyte reaction [14–16]. However, porous semiconductors with unidirectional elongated micro-order sized pores have never synthesized so far. Nakahata and Nakajima were succeeded in fabricating a lotus silicon by unidirectional solidification in a pressurized hydrogen atmosphere [17]. Different from the conventional nano-sized porous silicon, the pore size of the lotus silicon ranges from 10 μm to 1 mm in diameter. This type of porous silicon is considered to be novel porous semiconducting material. The lotus silicon with directional cylindrical gas pores was fabricated by unidirectional solidification through mold casting technique of the melt dissolving hydrogen in a pressurized hydrogen atmosphere.

Figure 6.12a shows an overview of lotus silicon fabricated in the hydrogen atmosphere of 0.21 MPa. Figure 6.12b, c shows the optical micrographs of the cross section perpendicular and parallel to the solidification direction, respectively. The pores in the cross section perpendicular to the solidification direction are round-shaped, while those parallel to the solidification direction are long and

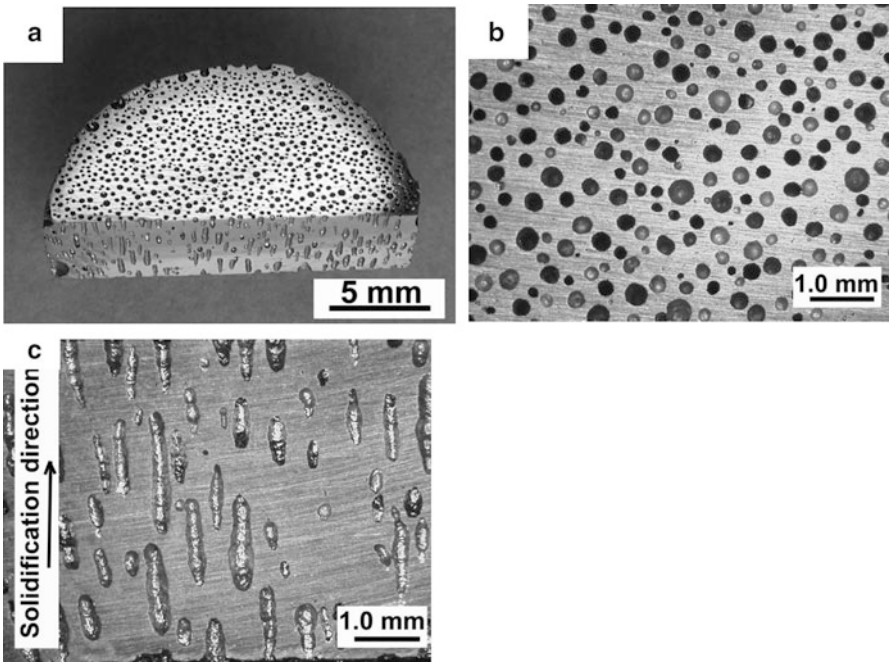

Fig. 6.12 (**a**) Overview and optical micrographs of cross section of lotus silicon overview, (**b**) cross section perpendicular to the solidification direction, and (**c**) cross section parallel to the solidification direction. The solidification occurred upward as shown in figure (**c**) (Reprinted with permission from [17]. © 2004 Elsevier B.V.)

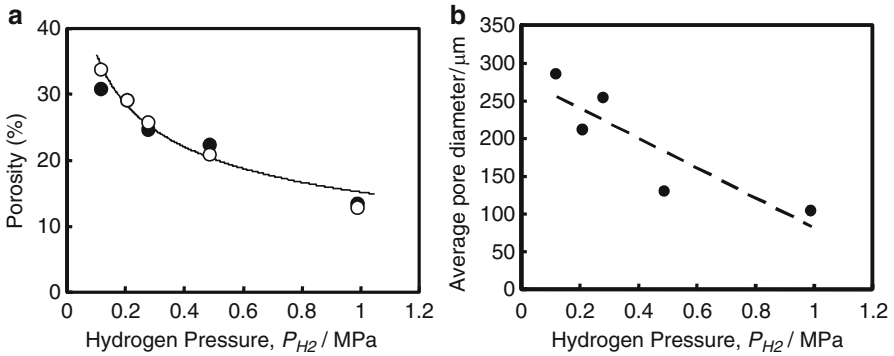

Fig. 6.13 (**a**) Porosity of lotus silicon as a function of hydrogen pressure: (*filled circle*) evaluated from apparent density of lotus silicon and (*open circle*) determined by the microstructural analysis of the cross sections at the distance 5 mm from the copper chiller. (**b**) Average pore diameter of the lotus silicon as a function of hydrogen pressure. The *closed circles* represent the average pore diameter determined by microstructural analysis of the cross sections at the distance 5 mm from the copper chiller and the *broken line* shows the fitted one by linear regression (Reprinted with permission from [17]. © 2004 Elsevier B.V.)

cylindrical. Figure 6.13a shows hydrogen pressure dependence of the porosity of the lotus silicon. The porosity decreases with increasing hydrogen pressure. Figure 6.13b shows hydrogen pressure dependence of the average pore diameter in the cross section on the sample plane at 5 mm in height from the bottom of the ingot. The pore diameter decreases with increasing hydrogen pressure; the pore size is about 100 μm in diameter at hydrogen pressure of 0.99 MPa. From Sieverts' law and Boyle's law, the following expression is derived:

$$V = \frac{(k_{\mathrm{l}} - k_{\mathrm{s}}) \times P_{\mathrm{H_2}}^{1/2} \times R \times T_{\mathrm{n}}}{2(P_{\mathrm{H_2}} + 2\sigma/r)}, \tag{6.5}$$

where k_{l} and k_{s} are the equilibrium constants of hydrogen dissolving reaction in liquid and solid, respectively. σ and r are the surface tension of the melt and pore radius. Since the surface tension of silicon at T_{n} (1,687 K) is about 0.74 Nm^{-1} [18] and the pore diameter in the range from 103 to 286 μm, the value of $2\sigma/r$ is estimated at most to be 0.03 MPa, which is in fact negligible small in comparison with the corresponding $P_{\mathrm{H_2}}$ of 0.99 MPa. Thus, the pore volume is inversely proportional to $P_{\mathrm{H_2}}^{1/2}$. The porosity increases by a factor of about 2.7 when the hydrogen pressure decreases from 0.99 to 0.12 MPa, which is in good agreement with the estimation by the above equation; the porosity increases by a factor of $(0.99/0.12)^{1/2} \approx 2.9$. Although the present evaluation is not exact because of neglecting some effect such as temperature gradient, the pore evolution behavior can be explained by supersaturation of hydrogen in the solidified silicon.

6.5 Fabrication of Lotus Alumina by Unidirectional Solidification

Porous oxide ceramics have been used as hot gas or molten metal filters and catalyst because of their excellent mechanical properties, high-temperature resistance, and chemical stabilities. Porous ceramics with highly oriented cylindrical pores are convenient to use as a gas filter and as a catalyst carrier. Ishizaki et al[19] suggested that the appropriate pore size for gas filter application is between 10 and several hundred micrometer. Hence, in the development of a gas filter, control of the pore size is an important issue. Several research groups have proposed to the fabrication processes of porous alumina with oriented cylindrical pores. Zhang et al. [20] fabricated porous alumina with unidirectionally aligned continuous pores via the slurry coating of fugitive cotton filter. Porous alumina with approximately 150-μm-diameter pores and 35 % porosity was fabricated using their method. Ding et al. [21] prepared a porous alumina with oriented pores by combining a foaming method with sol–gel technology. A porous alumina with 1-mm-diameter pores and 35 % porosity was fabricated from their method. Isobe et al. [22] prepared porous alumina with oriented cylindrical pores by an extrusion method. In their method, a porous alumina with 14-μm-diameter pores and 35 % porosity was fabricated. Fukasawa et al. [23] have developed a fabrication method for porous alumina with oriented pores using the freeze-drying technique. However, it is difficult to control the porosity and/or pore size of the porous alumina by these methods.

On the other hand, in the field of metals, porous metals with cylindrical pores called as lotus metals were proposed. The porous metals are fabricated by unidirectional solidification under pressurized hydrogen gas, utilizing the hydrogen solubility gap in between liquid and solid. For such metals, the phase diagrams for metal–hydrogen system have been established. However, data of hydrogen gas solubility in oxides are hardly available. Ueno et al. [24] investigated lotus alumina fabricated by unidirectional solidification under pressurized hydrogen gas to elucidate the formation mechanism of pores.

Feed rods were prepared by high-purity alumina powder (99.99 % purity). The powder was mixed with a binder in water and a green rod was prepared by the slip-casting method. After drying in air, calcination was performed at 1,473 K for 7.2 ks in air, and then, a feed rod with 8 mm in diameter and 150 mm in length was obtained. The solidification was carried out using an optical floating zone apparatus under pressurized hydrogen gas where 100%H_2 gas, 50%H_2-Ar mixture gas, or 10%H_2-Ar mixture gas was used as the environmental gas, as illustrated in Fig. 6.14. A xenon lamp was used as an optical source. The light from the xenon lamp was put on the focus by the elliptical mirror to set up the melting zone of the feed rod. The top of the feed rod was hooked on the upper shaft and the bottom was fixed to the lower shaft. The melting system was set up in a quartz tube. During the unidirectional zone melting, the solidification rate and the rod rotation were fixed to 200 mm h^{-1} and 20 rpm, respectively.

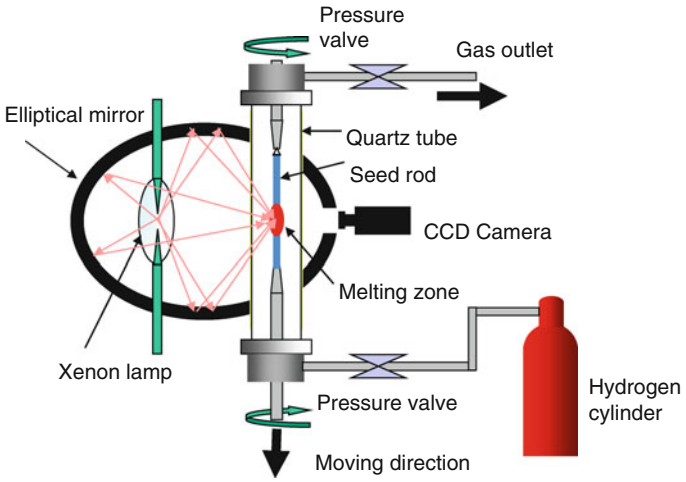

Fig. 6.14 Schematic drawing of fabrication apparatus for lotus ceramics

Lotus alumina was successfully fabricated by unidirectional solidification under a pressurized hydrogen atmosphere. Figure 6.15a, b shows transversal and longitudinal cross-sectional views of the solidified sample prepared in 100%H_2 gas under the pressure of 0.8 MPa. Many cylindrical pores were aligned along the solidification direction. Some large pores were seen in the inner periphery and in the center of the sample. In the longitudinal cross-sectional view, the large pores possessed a spherical shape, which is quite different from the morphology of cylindrical pores. Hence, it is considered that the formation mechanism of these two types of pores is different. For the cylindrical pores, which are the dominant pores found in the figure, the shape of the pores is very similar to that of lotus metals. Thus, this type of pore is formed at the solid–liquid interface during the solidification due to a hydrogen solubility gap between liquid and solid phases. One possible model for the formation of sphere-shaped pores is trapping gas bubbles that are released from the solid–liquid interface to the liquid phase by the solid phase during unidirectional solidification.

Figure 6.16 shows the total pressure dependence of the porosity in the samples prepared in 100%H_2, 50%H_2-Ar, and 10%H_2-Ar gases. For the samples prepared in 100%H_2, the porosity once increases with increasing the pressure up to 0.4 MPa and then gradually decreases. A similar tendency was observed for lotus copper. Yamamura et al. suggested that there are two factors controlling the porosity in the formation of lotus metals: Sieverts' law and Boyle's law [25]. It is known that the porosity of lotus metals is proportional to hydrogen partial pressure. However, the pressure inside the pore is driven by environmental pressure according to Boyle's law. Hence, the porosity decreases with increasing total pressure according to Boyles law. Thus, the porosity of lotus materials is determined by two contrary laws related to hydrogen partial pressure and total pressure. Because Ar gas cannot be dissolved into liquid and solid metal phases, Ar gas in the

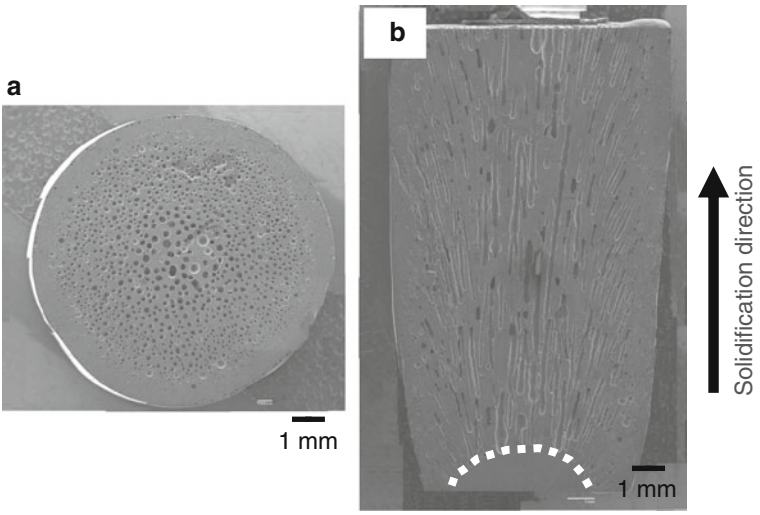

Fig. 6.15 Transversal cross-sectional and longitudinal cross-sectional views of the solidified sample prepared in mixed gas of 50%H_2-50%Ar at 0.8 MPa (Reprinted with permission from [24]. © 2007 The American Ceramic Society)

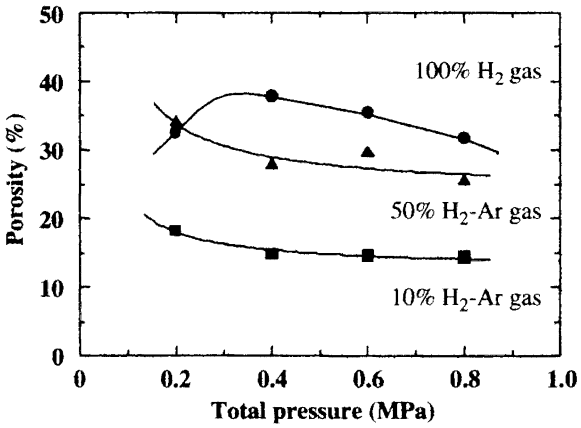

Fig. 6.16 Porosity changes in the samples prepared in 100%H_2, 50%H_2-Ar, and 10%H_2-Ar gases (Reprinted with permission from [24]. © 2007 The American Ceramic Society)

H_2-Ar mixture gas affects only to increase the total pressure so that the effect of Boyle's law became dominant. The same reasoning is also applied to lotus alumina as shown in Fig. 6.16.

Figure 6.17 shows the total pressure dependence of the average pore diameter of the samples. The pore size decreases with increasing total pressure of the gas, which is explained by Boyle's law. On the other hand, since the absolute amount of hydrogen gas increases with increasing hydrogen partial pressure, the pore volume increases with increasing hydrogen partial pressure.

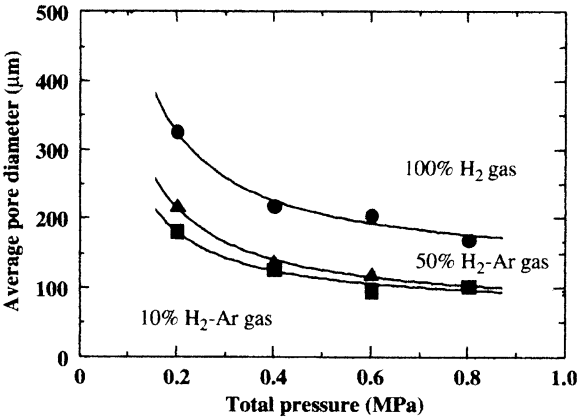

Fig. 6.17 Longitudinal cross-sectional views of the solidified sample prepared in 50%H_2-Ar gas at 0.8 MPa (Reprinted with permission from [24]. © 2007 The American Ceramic Society)

6.6 Fabrication of Lotus Brass by Solid-State Diffusion

It is not easy to fabricate lotus brass by unidirectional solidification method in gas atmosphere. This is probably because of its very small hydrogen solubility difference between solid and liquid of brass. Instead of solidification, lotus brass is fabricated by utilizing solid-state diffusion of zinc into porous copper which is made by unidirectional solidification in high pressure of hydrogen atmosphere [26]. The vapor deposition method is adopted; the lotus copper sample was wrapped in a tantalum foil and was annealed together with the zinc piece in a quartz tube with vacuum of 1×10^{-4} Pa. During annealing, zinc was evaporated, deposited onto the lotus copper, and diffused into the copper. After annealing, the samples were observed by an optical microscope and their compositions were analyzed by an electron probe microanalysis (EPMA).

Figure 6.18 is the result of the analysis by EPMA on the sample annealed at 953 K for 4.32×10^4 s. No zinc pieces remained in the quartz tubes after annealing. All of zinc atoms evaporated and diffused into the samples. It was found that the composition was almost constant between two neighboring pores on the cross section parallel to pore direction; the zinc concentration is around 40 at.% and almost uniform composition. Thus, the lotus brass was fabricated by zinc diffusion into lotus copper.

6.7 Effect of Microstructure on Pore Morphology in Lotus Magnesium Alloys

Magnesium is considered to be a rather new material as a lightweight structural metal. Usually the magnesium alloys are used for high-mechanical strength and good anti-corrosion resistance. As mentioned before, lotus magnesium can be produced by unidirectional solidification through the mold casting technique [27]. However,

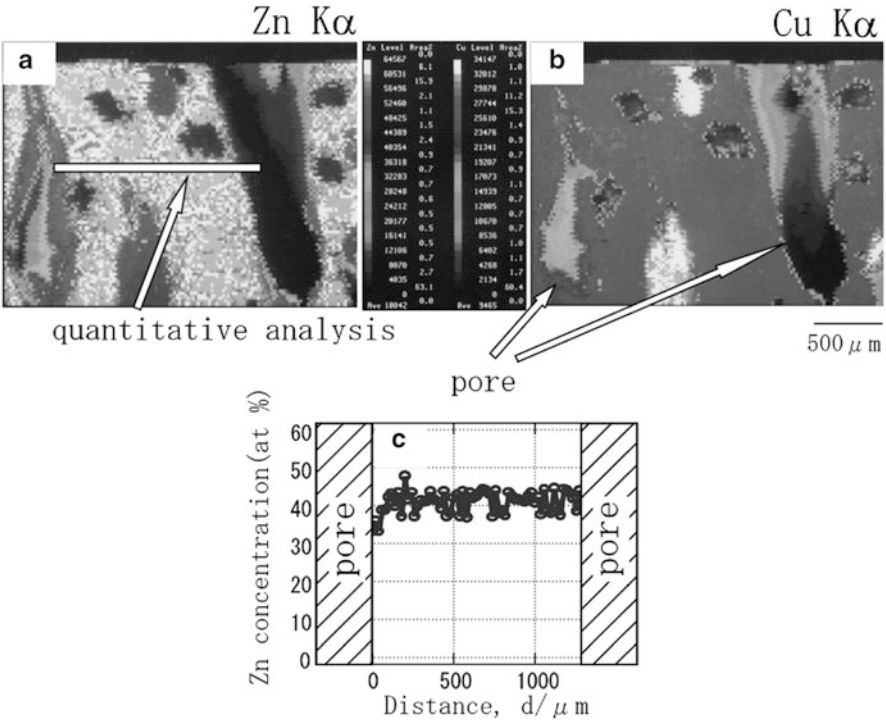

Fig. 6.18 Results of electron probe microanalysis in the samples annealed at 935 K for 4.32×10^4 s in a quartz tube with a zinc piece: (**a**) map of Zn Kα intensity, (**b**) map of Cu Kα intensity, and (**c**) composition–distance profiles between two pores (Reprinted with permission from [26]. © 2003 Japan Institute of Metals)

it was found by Hoshiyama et al. [28] that addition of alloying elements significantly changes the pore shape and the porosity. Three kinds of alloys, Mg-9%Al-0.75%Zn (AZ91D), Mg-3Al-1Zn (AZ31B), and Mg-3Al-0.25Zn (AZ91D), the latter of which is diluted with magnesium and is abbreviated as (1/3)AZ91D, were used. Figure 6.19 shows photographs on the longitudinal sections of porous (1/3)AZ91D, AZ31B, and AZ91D alloys. In the lower region near the bottom chiller of (1/3)AZ91D and AZ31B alloys, elongated pore growth is observed, while almost all pores in AZ91D alloy are spherical, not cylindrical. Comparing (1/3)AZ91D with AZ31B the pores in the former alloy are longer than that in the latter, because total concentration of the alloying elements is lower in the former. The number of pores and porosity decrease with increasing concentration of the alloying elements Al, Zn, and Mn. This result is explained in terms of the decrease in hydrogen solubilities in the magnesium alloys due to addition of alloying elements [29]. Figure 6.20 shows Mg-Al equilibrium phase diagram in magnesium-rich side. The temperature interval ΔT between liquidus and solidus lines at each composition increases by 43.5 K, 52.5 K, and 150 K in order

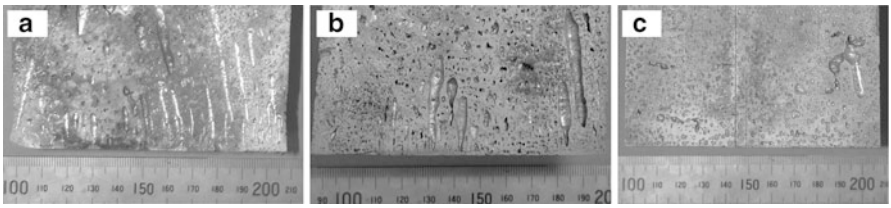

Fig. 6.19 Photographs on longitudinal sections of lotus magnesium alloys. (**a**) (1/3)AZ91D, (**b**) AZ31B, and (**c**)AZ91D alloys. Copper chiller was used for the bottom plate of the mold (Reprinted with permission from [28]. © 2008 Freund Publishing House Ltd)

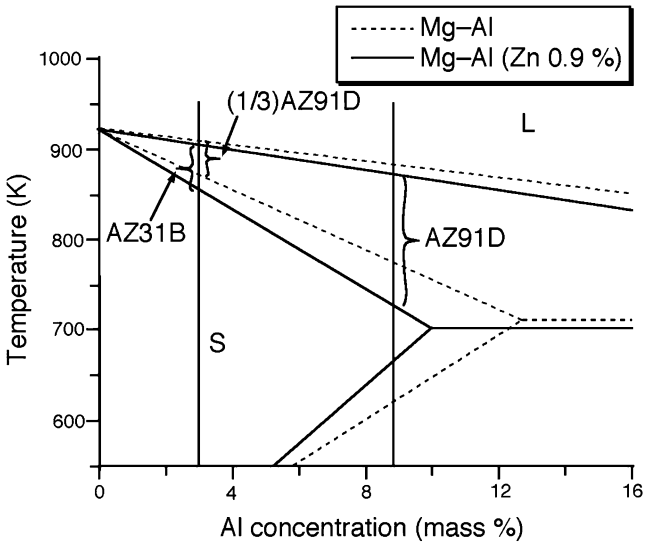

Fig. 6.20 Magnesium-rich side of Mg-Al equilibrium phase diagram (Reprinted with permission from [28]. © 2008 Freund Publishing House Ltd)

of (1/3)AZ91D, AZ31, and AZ91D, respectively; ΔT corresponds to increase in coexistence region of solid and liquid phases.

Let us think about pore growth mechanism in such mushy zone. When the alloy is solidified by way of the mushy zone, the ratio of solid phase portion in the mushy zone increases with decreasing temperature and the hydrogen rejected in the solid phase forms the pores. The schematic drawing of wide mushy zone is illustrated in Fig. 6.21a. Even if the pores are nucleated, the solid phase which is precipitated in front of evolved pores prevents the pores from growing toward the solidification direction. On the other hand, in the short mushy zone in Fig. 6.21b, the top of the cylindrical pores can grow without the precipitation of solid phase. Thus, it is concluded that the shorter the mushy zone is, the longer the pores grow.

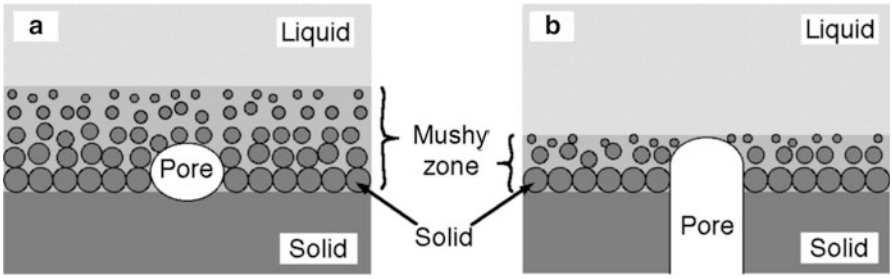

Fig. 6.21 Effect of the mushy zone on pore growth. Width of the mushy zone is (**a**) wide and (**b**) narrow. The mushy zone affects the pore evolution in unidirectional solidification (Reprinted with permission from [28]. © 2008 Freund Publishing House Ltd)

6.8 Fabrication of Lotus Carbon Steel by Continuous Casting Technique

Lotus carbon steel is suitable for lightweight high-strength structural material. For practical purpose, lotus carbon steel plates are expected to be used for movable structural bodies of machine tools because of the effects of reduction of weight and vibration damping, which improve the precision and productivity of machining, the tool life, etc. Although the continuous casting apparatus was used to fabricate lotus copper, magnesium, and aluminum, some modifications of the apparatus were required for fabrication of lotus carbon steel, because there are several problems as follows. Since iron reacts easily with carbon, nitrides, and so on, endurance of the refractory, a ceramic material which is not reactive with iron, was selected as the refractory. In order to improve the endurance of the refractory, a technique for a rigid connection among the crucible, the break ring, and the mold was developed [30]. The second problem was the friction between the mold and the carbon steel, which causes the blockage of melt in the mold during continuous casting. To solve this problem, intermittent motion was adopted, where a cycle of transfer and stop is repeated periodically. This technique can give a vibration to the carbon steel sample in order to deduce the friction. In the following sections, transfer velocity means the average value, which is the transfer distance per unit time over several cycles as shown in Fig. 6.22. By developing this technique, it became possible to fabricate long lotus carbon steel up to 600 mm in length.

Figure 6.23 shows the fabricated lotus carbon steel at 100 mm min^{-1}. On the surface, ripple marks are observed periodically. These ripple marks were generated at each cycle of the intermittent motion and correspond to the solid–liquid interface. The ripple marks show that the solid–liquid interface changed from horizontal to concave shape with a depth h during the continuous casting. The change can be explained by the position of interface, which is considered to have dropped during continuous casting, because cooling capacity of the mold was not enough to solidify the total amount of the melt, which entered during one cycle. The length of the

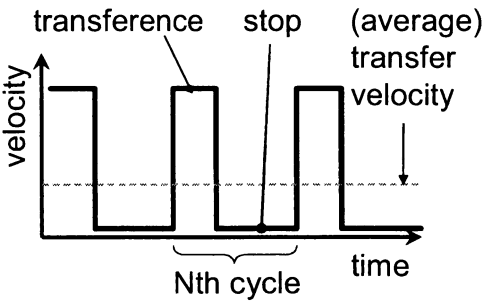

Fig. 6.22 Intermittent motion of transfer (Reprinted with permission from [30]. © 2007 MIT-Verlag)

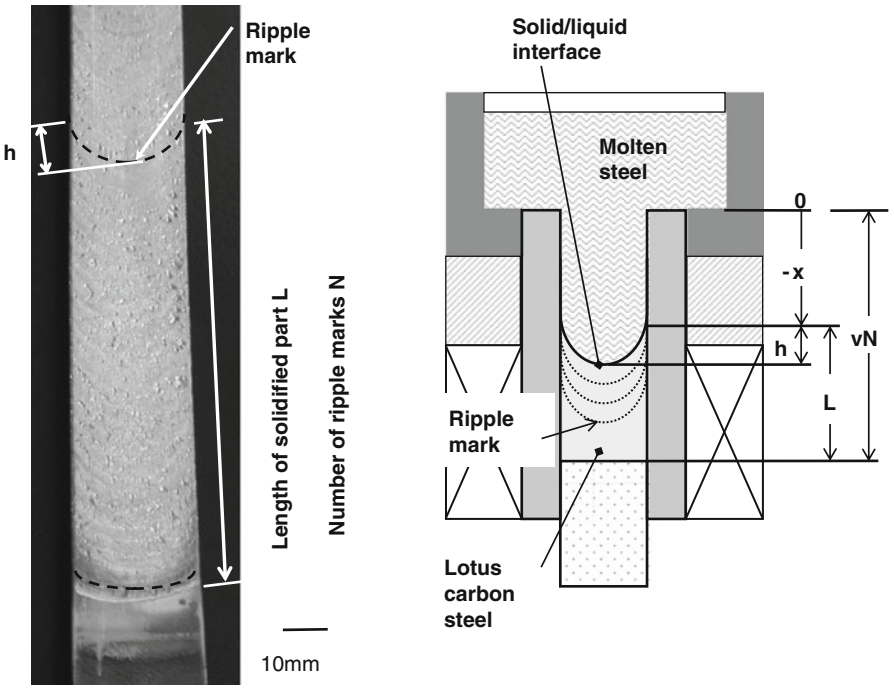

Fig. 6.23 Fabricated lotus carbon steel. (*left*) *Ripple mark* on the surface of solidified slab of lotus carbon steel. (*right*) Schematic drawing around the solid/liquid interface during continuous casting (Reprinted with permission from [30]. © 2007 MIT-Verlag)

solidified part L until the Nth cycle (see Fig. 6.22) was measured by the ripple mark. Then, the position of the solid/liquid interface can be evaluated by the difference between L and vN, which is the moving distance of the dummy bar, where v is a moving distance per a cycle.

Figure 6.24 shows the measured position and depth of the solid–liquid interface at each cycle in the experiment of 100 mm min^{-1}. At the beginning of the continuous casting, the position is close to the crucible. The small h-value shows that the interface is nearly horizontal. In this case small pores are distributed.

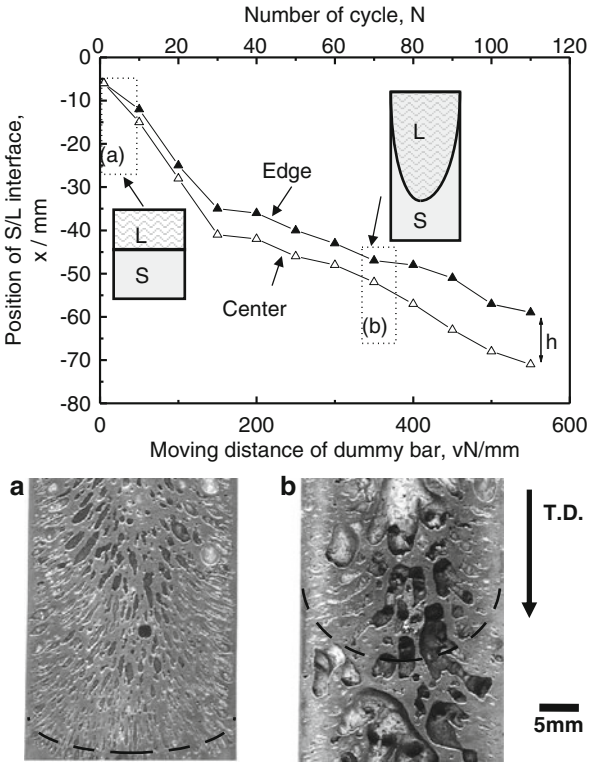

Fig. 6.24 Position of the solid–liquid interface at each cycle number. The pictures show the cross sections parallel to the transfer direction at the initial transference (**a**) and at about 80 cycles (**b**). The *dotted lines* show the solid–liquid interface (Reprinted with permission from [30]. © 2007 MIT-Verlag)

With increase of the cycle number, the position dropped and the interface became a deep concave shape with a large value of h. In this case coarsened irregular pores are observed.

The mechanism of these results is illustrated in Fig. 6.25. In the initial state (a), the melt is cooled mainly by the heat flow in the longitudinal direction, because this is a heating zone. Then the solid–liquid interface is horizontal. But if the solid–liquid interface is located in the cooling zone (b), the heat flow is mainly in the width direction and the interface becomes concave. As the pores grow perpendicular to the solid–liquid interface, the pores merge with each other in the center. Coarsened irregular pores are generated.

From these results the mechanism of pore formation depending on the transfer velocity became clear as shown in Fig. 6.26. Then one can find the condition for small pores distributed homogeneously at around 20 mm min^{-1}.

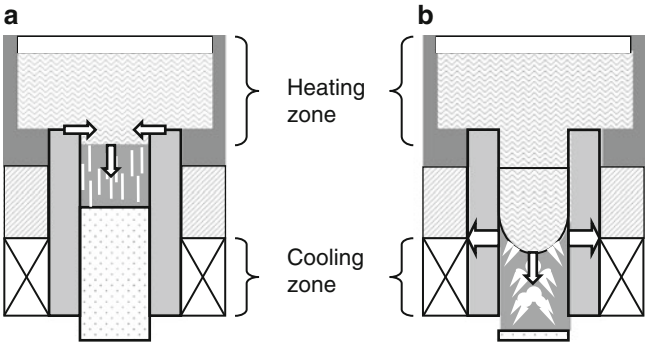

Fig. 6.25 Mechanism of the descent position of the solid–liquid interface and he change into a concave shape. (**a**) The initial transference and (**b**) after several ten cycles (Reprinted with permission from [30]. © 2007 MIT-Verlag)

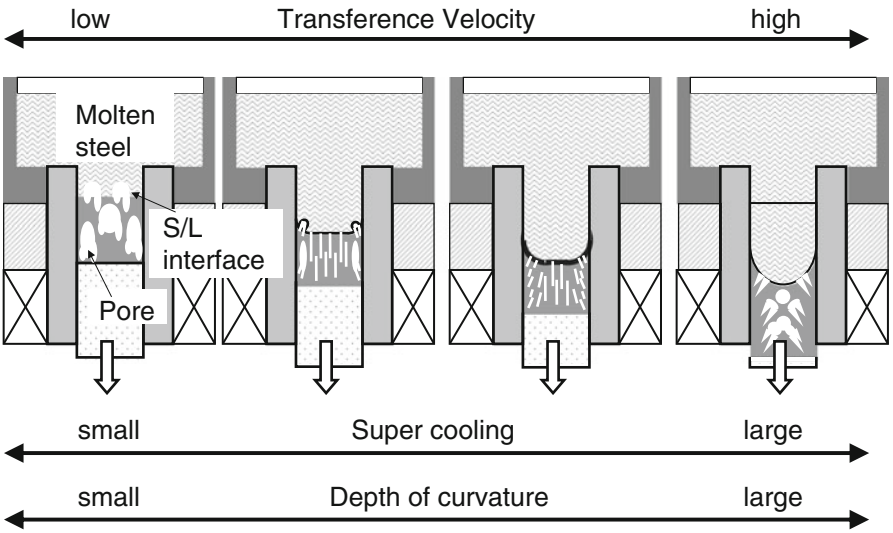

Fig. 6.26 Schematic illustration of the dependence of pore formation on transfer velocity (Reprinted with permission from [30]. © 2007 MIT-Verlag)

6.9 Fabrication of Lotus Aluminum by Continuous Casting Technique

Lotus aluminum possessing slender directional pores aligned in one direction is one of the most promising candidates for lightweight structural materials [31]. Numerous investigations have focused on the fabrication of porous aluminum and its alloys with slender directional pores formed by unidirectional solidification in a hydrogen atmosphere. Particularly, solidification defects have been emphasized for

Table 6.1 Previously reported porosity and pore size results in lotus aluminum fabricated in hydrogen atmosphere

Materials (mass%)	Atmosphere (H_2/MPa)	Pore diameter (μm)	Porosity (%)	First author (year) [ref]
Al (99.8%pure)	0.1		<1.6	Shinada (1980) [32]
Al	0.05	40-60	0.2	Shahani (1985) [33]
	0.1	50-60	0.9	
	0.3	125-150	0.6	
	0.5	150-200	1.1	
Al	0.11	difficult to produce regular high-porosity Al		Shapovalov (1993) [34]
Al-(2-8)%Fe	0.11	Al_3Fe precipitates promote pore formation		
Al	0.1	60	5.1	Zhang (2007) [35]
	$0.18H_2$+0.22Ar	75	<0.1	
	air	60	0.1	
	air	60	0.3	

basic and applied research of a lightweight material. Table 6.1 is a compilation of these works [32–35]. None of the previous works produced porous aluminum with directional pores and a high porosity; the porosity is limited to 5 % at most.

Lotus aluminum can be fabricated utilizing the hydrogen solubility gap between a liquid and a solid at the melting point in the unidirectional solidification process in a hydrogen atmosphere. When the melt dissolving hydrogen is solidified, the insoluble hydrogen is precipitated to evolve directional pores in the solidified region at the solid–liquid interface. Therefore, the following conditions are critical to fabricate highly porous lotus metals.

1. The hydrogen concentration dissolved in the molten metal should exceed several atomic percent.
2. The metal should hold a smaller solid solubility of hydrogen so that the solubility gap between liquid and solid metals becomes larger.

However, the hydrogen solubility in liquid and solid aluminum [36] is only about 2 % of those for magnesium, copper, and transition metals [37, 38]. Consequently, previous researchers considered the fabrication of highly porous lotus aluminum difficult; none of the previous reports successfully fabricated lotus aluminum with a porosity above 5 %.

The influence of solidification conditions (solidification velocity, hydrogen partial pressure, temperature gradient, and melt temperature) on pore formation of lotus aluminum was experimentally and theoretically investigated by Ide et al. [39] to elucidate the pore formation mechanism as well as to control porosity. They fabricated lotus aluminum with slender unidirectional pores using a continuous casting technique under controlled solidification conditions. In particular, it was clarified that the porosity and the pore size are affected significantly by the solidification velocity as the velocity decreases the porosity and pore size by one

to two orders of magnitude compared to those for copper, magnesium, and transition metals. Based on this knowledge, lotus aluminum with a porosity as high as 40 % was obtained for the first time.

A continuous casting technique was utilized for unidirectional solidification in a pressurized hydrogen atmosphere under controlled solidification conditions. The temperature of the melt in the crucible was measured using two WRe 5/26-type thermocouples located 5 mm from the bottom of the crucible. Then to solidify the melt in a continuous downward direction, a graphite dummy bar pulled molten aluminum through a cooling mold at a constant solidification velocity. The solidification temperature using two K-type thermocouples inserted in the graphite dummy bar. To ensure the temperature gradient was at a steady state, the temperature was measured 20 mm above the top of the dummy bar. The measured temperature was recorded every second using a temperature recorder (Keyence Co., Ltd.; GR-3500). The temperature gradient was calculated using the obtained cooling curve in the temperature range from 933 to 873 K (temperature−time curve). The temperature gradient was determined using the following equation:

$$G = \frac{V}{R}, \tag{6.6}$$

where G, V, and R are the temperature gradient (K mm^{-1}), cooling rate during unidirectional solidification (K s^{-1}), and solidification velocity (mm s^{-1}), respectively. The temperature gradient was determined from the average of two temperature gradients, whose difference was less than 0.3 K mm^{-1}).

The effects of different characteristics on pore morphology were examined. The influence of the solidification rate was probed by melting pure aluminum and unidirectionally solidifying in a mixture of hydrogen 0.25 MPa and argon 0.25 MPa with a constant temperature gradient and melt temperature of 9.7 K mm^{-1} and 1,223 K, respectively, while changing the solidification velocity from 0.5 to 0.9 mm min^{-1}. The impact of hydrogen partial pressure was investigated by melting aluminum and unidirectionally solidifying in three different atmospheres: hydrogen 0.5 MPa, argon 0.5 MPa, or mixed gas (0.5 MPa) consisting of hydrogen (0.25 MPa) and argon (0.25 MPa) when the solidification velocity, temperature gradient, and melt temperature were set to 0.9 mm min^{-1}, 9.5 K mm^{-1}, and 1,223 K, respectively.

Figure 6.27 shows the typical pore morphology perpendicular (upper row) and parallel (lower row) to the solidification direction of lotus aluminum as a function of solidification velocity from 0.5 mm min^{-1} to 0.9 mm min^{-1}. Lotus aluminum was fabricated by unidirectional solidification in a mixture of hydrogen (0.25 MPa) and argon (0.25 MPa). Figure 6.27f shows an outer view of lotus aluminum with the highest porosity of nearly 40 %. Unidirectional pores aligned parallel to the solidification direction are observed in the solidified lotus aluminum. The porosity and average pore diameter decrease as the solidification velocity increases.

Figure 6.28 shows the pore morphology in lotus aluminum fabricated by unidirectional solidification at a solidification velocity of 0.9 mm min^{-1} as a function of

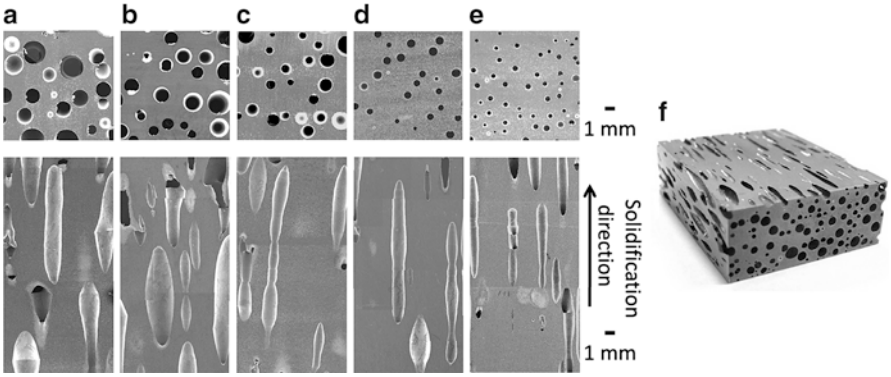

Fig. 6.27 Cross sections perpendicular (*upper row*) and parallel (*lower row*) to the solidification direction of lotus aluminum. Solidification velocity: (**a**) 0.5 mm min^{-1}, (**b**) 0.6 mm min^{-1}, (**c**) 0.7 mm min^{-1}, (**d**) 0.8 mm min^{-1}, and (**e**) 0.9 mm min^{-1}. (**f**) Outer view of lotus aluminum with the highest porosity of nearly 40 %

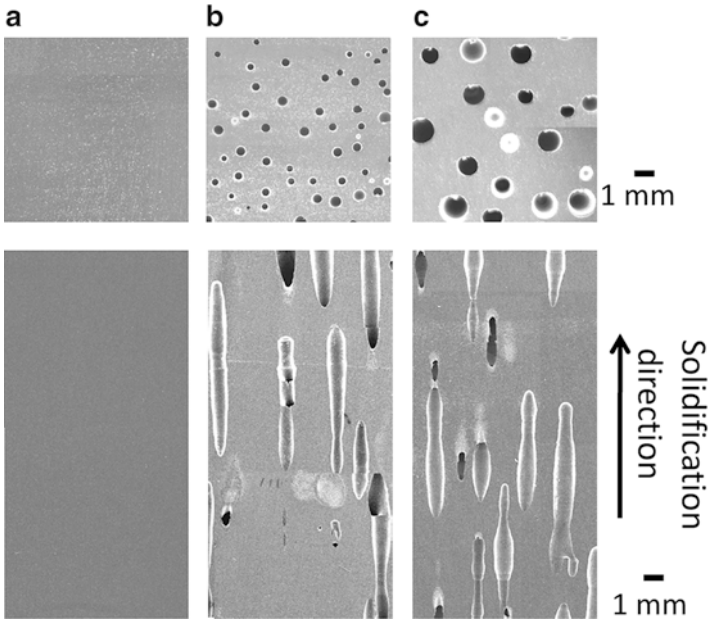

Fig. 6.28 Cross sections perpendicular (*upper row*) and parallel (*lower row*) to the solidification direction of lotus aluminum fabricated in different atmospheres: (**a**) argon (0.5 MPa), (**b**) mixed gas of hydrogen (0.25 MPa) and argon (0.25 MPa), and (**c**) hydrogen (0.5 MPa). Temperature gradient and melt temperature are 9.5 K mm^{-1} and 1,223 K, respectively

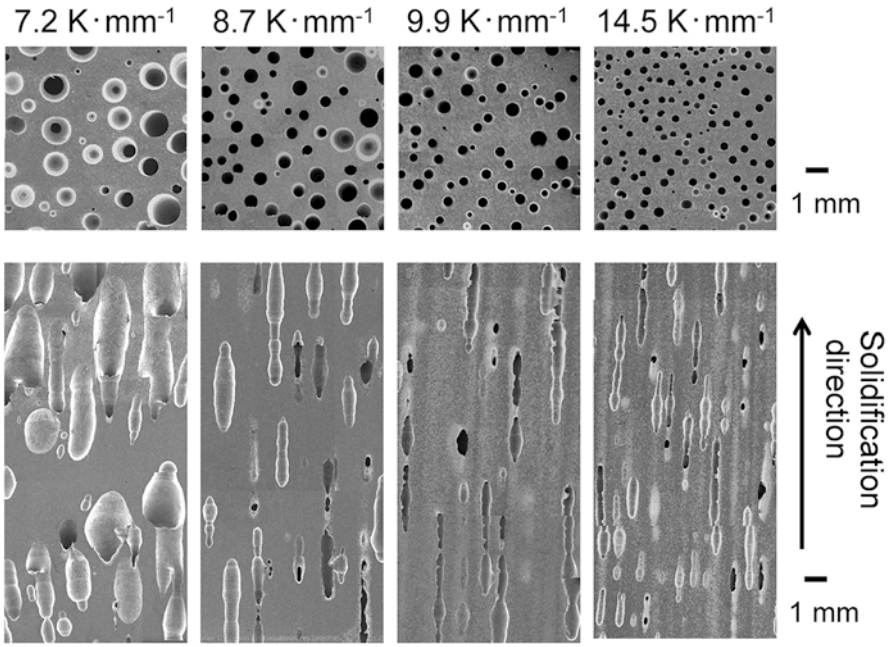

Fig. 6.29 Cross sections perpendicular (*upper row*) and parallel (*lower row*) to the solidification direction of lotus aluminum fabricated with different temperature gradients at the solid–liquid interface. Lotus aluminum is fabricated in a mixed gas of hydrogen (0.5 MPa) and argon (0.5 MPa) at a melt temperature of 1,373 K and a fixed solidification velocity of 0.5 mm min^{-1}

the hydrogen partial pressure; photos in the upper and lower rows are the cross-sectional views perpendicular and parallel to the solidification direction, respectively. The atmospheric total pressure was kept constant at 0.5 MPa, while the partial pressure of hydrogen was either zero, 0.25 MPa, or 0.5 MPa and the partial pressure of argon was 0.5, 0.25 MPa, or zero, respectively. The ingot solidified in an argon atmosphere does not exhibit pores (Fig. 6.28a). In contrast, ingots prepared in a hydrogen atmosphere contain pores (Fig. 6.28b, c). It is apparent that dissolving gas in the melt is responsible for the evolution of pores, because hydrogen but not argon can dissolve in molten aluminum. Porosity and pore diameter increase as the hydrogen partial pressure increases.

Figure 6.29 shows cross-sectional views of the pore morphology perpendicular and parallel to the solidification direction of lotus aluminum fabricated at different temperature gradients. The porosity and average pore diameter decrease as the temperature gradient increases. Figure 6.30 shows the change in pore morphology due to the difference in the melt temperature of lotus aluminum fabricated with a solidification velocity of 0.9 mm min^{-1} in a 0.5 MPa hydrogen atmosphere. The porosity and average pore diameter increase as the melt temperature increases.

As mentioned above, the porosity of lotus aluminum depends on not only hydrogen partial pressure but also the solidification velocity, temperature gradient, and melt

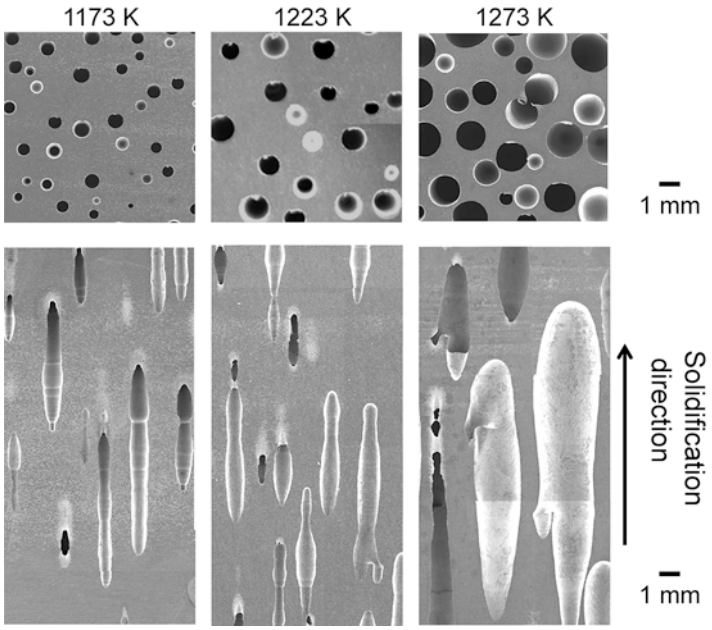

Fig. 6.30 Dependence of porosity and pore diameter on melt temperature of lotus aluminum fabricated with solidification velocity of 0.9 mm min^{-1} in 0.5 MPa hydrogen. Temperature gradient is 9.5 ± 0.5 K mm^{-1}

temperature. These dependencies are similar to those of dual-phase formation in eutectic alloys; the flux of solute atoms due to solidification conditions affects the morphology of the phases. This suggests that a change in the hydrogen flux by different solidification conditions significantly affects pore formation in lotus aluminum.

The solubility difference of hydrogen in aluminum is more than one order of magnitude smaller than that in copper, whereas the diffusion coefficients are similar in both aluminum and copper. To promote pore growth in lotus aluminum, hydrogen in aluminum should diffuse over a longer distance than in copper because the solubility of hydrogen is lower in aluminum. Figure 6.31 schematically depicts the effect of a long diffusion distance of hydrogen rejected in a solid in the vicinity of the solid–liquid interface on pore evolution in lotus aluminum. Assuming the diffusion distance of hydrogen increases, the porosity and pore diameter in lotus aluminum increase as the number of hydrogen atoms increases, resulting in the formation and growth of pores. Thus, the mechanism for pore evolution in lotus aluminum may be the opposite of the mechanism for lotus copper and stainless steel where the formation and growth of pores easily occur even for short distant diffusion of hydrogen due to the high content of hydrogen rejected in the solid. Therefore, the condition of a lower solidification velocity is certainly crucial to realize highly porous lotus aluminum.

The porosity and pore diameter decrease as the solidification velocity and temperature gradient increase, but increase as the hydrogen partial pressure and

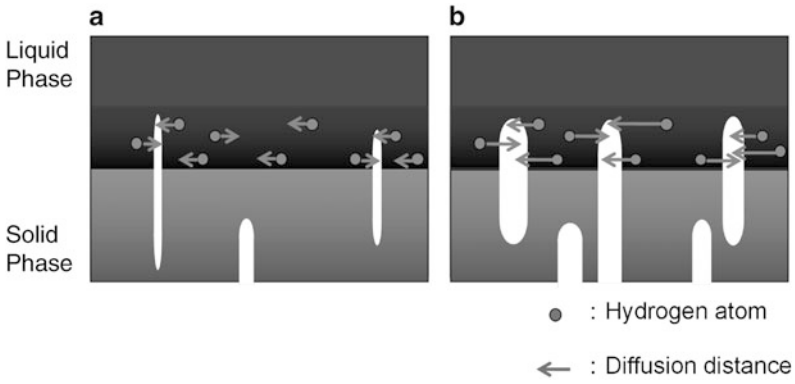

Fig. 6.31 Two-dimensional model for the growth of unidirectional pores near the liquid–solid interface. Hydrogen rejected in solidified aluminum accumulates in the liquid near the liquid–solid interface. (**a**) When the solidification velocity is fast, hydrogen diffuses only a short distance. Consequently, the impact of hydrogen on growth is small, leading to small pores and a low porosity. (**b**) When the solidification velocity is slow, hydrogen diffuses over a longer distance. Because a large amount of hydrogen contributes to growth, large pores and a high porosity are obtained

melt temperature increase. Previous works have reported the effects of solidification velocity and hydrogen partial pressure on pore formation of lotus metals. However, the influence of solidification velocity on pore formation in lotus aluminum differs from previous reports using other lotus metals such as copper [25] and stainless steel [40]. Similar to the fabrication of lotus copper or stainless steel, the pore diameter decreases as the solidification velocity increases. However, unlike for lotus aluminum, the porosity for lotus copper or stainless steel is independent of solidification velocity. Such a difference is attributed to the hydrogen solubility between the liquid and solid phases. For example, the hydrogen solubility gap between the liquid and solid phases in aluminum (4.93×10^{-4} mol% under H_2 0.1 MPa [36]) is about 40 times smaller than that of copper (2.09×10^{-2} mol% at H_2 0.1 MPa [37]), but there is not a significant difference in the diffusion coefficients [41, 42]. Therefore, the supersaturated hydrogen atoms in aluminum have to migrate a relatively long distance toward the pores to contribute to pore formation and growth. For a fast solidification velocity, the hydrogen atoms in aluminum cannot migrate a sufficient distance to grow large pores. On the other hand, for a slow solidification velocity, the hydrogen atoms in aluminum can migrate a longer distance, allowing more supersaturated hydrogen atoms to contribute to pore formation and growth, producing a larger porosity.

Next, we discuss effects of a hydrogen flux, which depends on the solidification conditions, on pore formation in lotus aluminum. In eutectic alloys, the morphology of a lamellar or rod structure is affected by solidification conditions. Such a change is due to the change in the flux of the solute. For a binary system composed of metal and hydrogen, we consider a dual phase, which consists of a combination of pores and aluminum. Figure 6.32 shows a two-dimensional model for the competitive

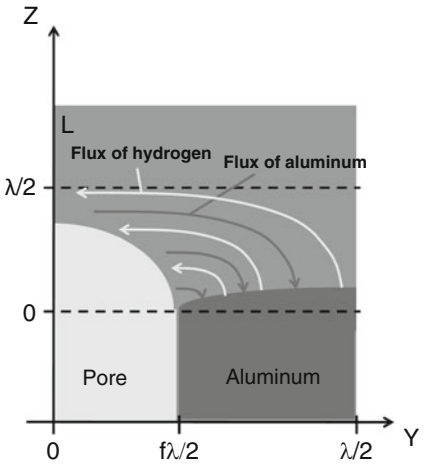

Fig. 6.32 Schematic drawing of the diffusion flux of hydrogen and aluminum during pore evolution and growth in the solidification front

growth between directional pores and solid aluminum under steady-state conditions. Ide et al. [39] treated the dual phase in two dimensions, and due to symmetry, only half of a lamellae for each phase needs to be considered [43]. As shown in Fig. 6.32, aluminum rejects hydrogen atoms due to the solubility gap in the melt, whereas the pore rejects aluminum atoms during unidirectional solidification. As well as the solute distribution in the eutectic structure, the mass of diffusing hydrogen (aluminum) atoms into pore (aluminum) per unit of time can be obtained by solving the diffusion equation for solute in the diffusion layer at the solidification front. Therefore, when the z-axis is parallel to the solidification direction and the y-axis is perpendicular to the solidification direction in the $y-z$ coordinate system (Fig. 6.32), the distribution of the solute concentration at the solidification front can be expressed by [43]

$$C = C_0 + A\ \exp\left(\frac{-Vz}{D}\right) + B\ \exp\left(\frac{-2\pi z}{\lambda}\right)\cos\left(\frac{-2\pi y}{\lambda}\right), \tag{6.7}$$

where C_0 and D are concentration (mol) and diffusion coefficient ($m^2\ s^{-1}$) of solute in molten metal, respectively, V is the growth velocity ($m\ s^{-1}$), and λ is the distance between periodic phase structure (m). Here A and B are, respectively,

$$A = f\left(C_S^{\beta} - C_S^{\alpha}\right) + C_E - C_S^{\beta}, \tag{6.8}$$

$$B = \frac{f(1-f)V\lambda\left(C_S^{\beta} - C_S^{\alpha}\right)}{2D\sin(\pi f)}, \tag{6.9}$$

where f is the volume fraction of theαphase, C_S^{α} and C_S^{β} are the solid solubility limit of B atoms in the α and β phases (mol m^{-3}), respectively. When B atoms are

rejected by the α phase and diffuse into the β phase through $y = f\lambda/2$, the flux of B atoms, J (mol s^{-1} m^{-2}) is obtained by

$$J = -D\left(\frac{\partial C}{\partial y}\right)_{y=\frac{f\lambda}{2}} = \pi f(1-f)V\left(C_S^{\beta} - C_S^{\alpha}\right)\exp\left(-\frac{2\pi z}{\lambda}\right). \tag{6.10}$$

Here, the width of the inspissated solute layer (diffusion layer) is considered to be about $\lambda/2$. When a small distance dl is solidified, the amount of diffusing hydrogen, C_{dl} (mol m^{-1}), into the nearby phase through the small Δl is given by

$$J_{dl} = \int_0^{\lambda/2} Jdz \times \frac{dl}{V} = f(1-f)\left(C_S^{\beta} - C_S^{\alpha}\right)\lambda dl, \tag{6.11}$$

where α and β are the aluminum and pore phases, respectively, and A and B atoms denote aluminum and hydrogen atoms, respectively. C_α and C_β are the hydrogen solubility in solid aluminum and the gas phase (mol m^{-3}), respectively. Because solid aluminum is not dissolved in the gas phase, the molar ratio of hydrogen is equal to 1. Therefore, C_α and C_β are expressed as

$$C_\alpha = \frac{\eta_{T_n}}{V_{Al}} \times \sqrt{P_{H_2}}, \tag{6.12}$$

$$C_\beta = \frac{2RT_n}{P} \times \sqrt{P_{H_2}}. \tag{6.13}$$

Here the volume fraction in the equilibrium phase diagram is used as the volume fraction f. However, because the porosity of lotus aluminum depends on the solidification conditions, the volume fraction of aluminum phase f is obtained from the experimental results. In the present work, Yamamura's model for mass balance of lotus copper [25] is modified by considering hydrogen diffusion, i.e., the terms indicating the mass of hydrogen are substituted using Eqs. (6.9)–(6.11).

[Initial amount of hydrogen contained in the liquid in the volume element]
+ [Amount of hydrogen contained in the liquid flowing into the volume element to compensate for solidification shrinkage]
– [Amount of hydrogen contained in the liquid flowing out of the volume element due to pore formation]
+ [Amount of hydrogen dissolved in solid copper around the pore with a length of $l + dl$].

In Yamamura's model, the hydrogen mass balance for a unit length as the solidification front advances dl is considered. Because the number of pores per unit length and supplied hydrogen from both sides of the pores have to be considered as the solidification front advances dl, the mass of diffusing hydrogen is written as

$$W_H = f(1-f)\left(C_\beta - C_\alpha\right)\lambda \times \frac{2}{\lambda} \times \frac{M}{2} dl \tag{6.14}$$

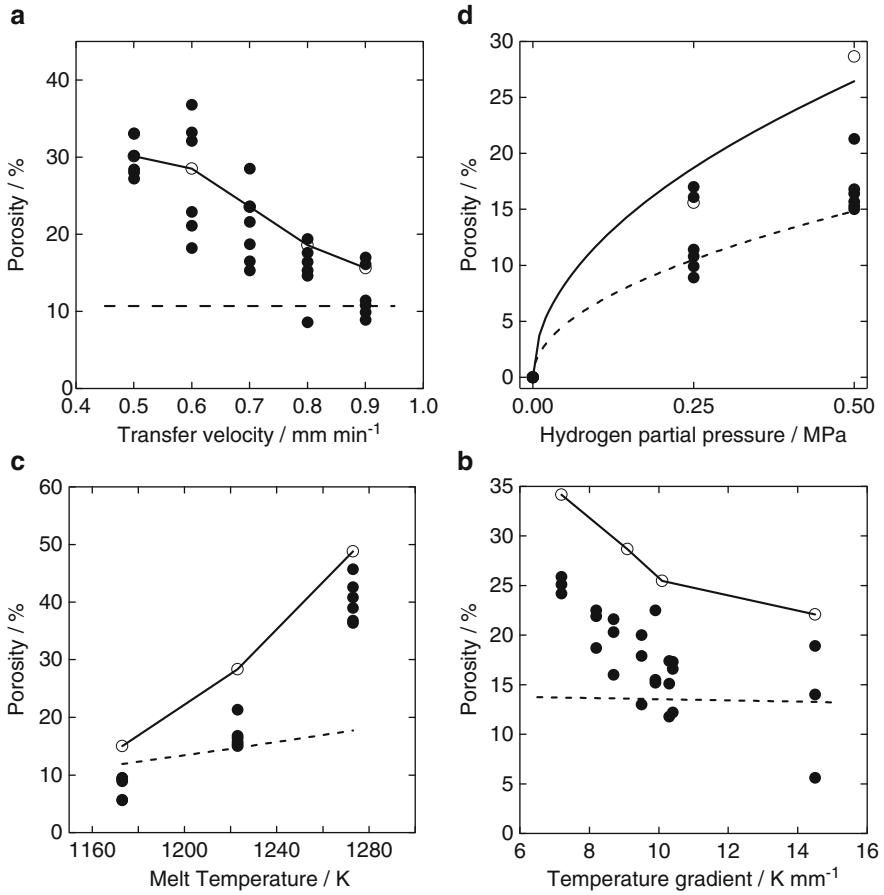

Fig. 6.33 Dependence of porosity on (**a**) solidification velocity, (**b**) hydrogen partial pressure, (**c**) melt temperature, and (**d**) temperature gradient. *Closed* and *open circles* indicate experimental data and the calculated results using Eq. (6.16), respectively. *Dotted lines* are the predicted results using Yamamura's model

In the present work, λ is given by following equation using porosity ε (%) where pore diameter d_p (m) given by experimental results:

$$\lambda = \frac{d_p}{\varepsilon}. \tag{6.15}$$

Equation (6.14) is substituted in Yamamura's model and the porosity of lotus metal is expressed as

$$\varepsilon = \frac{fM(1-f)\left(C_\beta - C_\alpha\right) + \left(\eta_{T_n} - \eta_{T_n-Gl}\right)\sqrt{P} \times \frac{M}{2V_{Al}}}{\frac{MP}{R(T_n-Gl)} + \left(\eta_{T_n} - \eta_{T_n-Gl}\right)\sqrt{P} \times \frac{M}{2V_{Al}}} \tag{6.16}$$

Figure 6.33 shows the dependence of porosity on (a) solidification velocity, (b) hydrogen partial pressure, (c) melt temperature, and (d) temperature gradient.

To compare the experimental results and the calculated results predicted using Eq. (6.16) with Yamamura's model [25], closed circles, open circles, and the dotted line denote the experimental results, calculated results using Eq. (6.16), and the results predicted by Yamamura's model, respectively. The calculated porosities using Eq. (6.16) agree well with the experimental results. In Yamamura's model, the porosity was calculated by assuming that all of the rejected hydrogen atoms due to the solubility gap form pores; parameter $a = 1$. Although the dependence of the porosity calculated from Yamamura's model on the hydrogen partial pressure is consistent with the experimental results, the dependence of the porosity for the other factors using Yamamura's model is inconsistent with the experimental results. These observations are reasonable because Yamamura's model does not consider the effect of the solidification condition.

Moreover, even if all of hydrogen atoms rejected in the solidified metal evolve into pores, the maximum porosity calculated by Yamamura's model is less than 15 %, which is far below the maximum experimental porosity of 40 %. This discrepancy suggests that the contribution of hydrogen diffusion in the melt rejected in the solid phase near the solid–liquid interface is critical. Thus, control of solidification conditions such as the solidification velocity, hydrogen partial pressure, temperature gradient, and melt temperature is crucial to increase the porosity of lotus metal with a low hydrogen solubility.

References

1. Simmons JW (1996) Mater Sci Eng A 207:159–169
2. Hyun SK, Nakajima H (2002) Mater Trans 43:526–531
3. Satir-Kolorz AH, Feichtinger HK (1991) Z Metallkde 82:689–697
4. Levinsky Y (ed) (1997) Pressure dependent phase diagrams of binary alloys. ASM International, Materials Park, p 693
5. Raghaban V (ed) (1987) Phase diagram of ternary iron alloys. Indian Inst Tech, Delhi, p 143
6. Shah ID, Parlee NAD (1967) Trans AIME 239:763–764
7. Nakahata T, Nakajima H (2005) Mater Trans 46:587–592
8. Hoshiyama H, Ikeda T, Murakami K, Nakajima H (2003) J Jpn Inst Metals 67:714–720
9. Hirano T (1990) Acta Metall 38:2667–2671
10. Yamaguchi M, Inui H, Ito K (2000) Acta Mater 48:307–322
11. Deevi SC, Sikka VK (1996) Intermetallics 4:357–375
12. Hyun SK, Ikeda T, Nakajima H (2004) J Jpn Inst Metals 68:39–42
13. Lange KW, Schenck H (1969) Z Metallkd 60:638
14. Turner DR (1958) J Electrochem Soc 105:402–408
15. Unagami T, Seki M (1978) J Electrochem Soc 125:1339–1344
16. Cullis AG, Canham LT (1991) Nature 353:335–338
17. Nakahata T, Nakajima H (2004) Mater Sci Eng A 384:373–376
18. Przyborowski M, Hibiya T, Eguchi M, Egry I (1995) J Cryst Growth 151:60–65
19. Ishizaki K, Komarneni S, Nanko M (1998) Porous materials: process technology and applications, Materials technology series. Kluwer, Dordrecht
20. Zhang GJ, Yang JF, Ohji T (2001) J Am Ceram Soc 84:1395–1397
21. Ding XJ, Zhang JZ, Wang RD, Feng CD (2002) J Eur Ceram Soc 22:411–414
22. Isobe T, Tomita T, Kameshima Y, Nakajima A, Okada K (2006) J Eur Ceram Soc 26:957–960

23. Fukasawa T, Deng ZY, Ando M, Ohji T (2001) J Ceram Soc Jpn 109:1035–1038
24. Ueno S, Lin LM, Nakajima H (2008) J Am Ceram Soc 91:223–226
25. Yamamura S, Shiota H, Murakami K, Nakajima H (2001) Mater Sci Eng A318:137–143
26. Aoki T, Ikeda T, Nakajima H (2003) Mater Trans 44:89–93
27. Ikeda T, Nakajima H (2002) J Jpn Foundry Eng Soc 74:812–816
28. Hoshiyama H, Ikeda T, Nakajima H (2007) High Temp Mater Process 26:303–316
29. Watanabe T (1976) Light Metals 25:167
30. Kashihara M, Yonetani H, Suzuki S, Hyun SK, Kim SY, Kawamura Y, Nakajima H (2007) Porous metals and metallic foams. MIT, Boston, pp 201–204
31. Nakajima H (2010) Proc Jpn Acad Ser B 86:884–899
32. Shinada H, Nishi S (1980) J Jpn Inst Light Metals 30:317–323
33. Shahani H, Fredriksson H (1985) Scand J Metall 14:316–320
34. Shapovalov VI, Timchenko AG (1993) Phys Met Metall 76:335–337
35. Zhang H, Li Y, Liu Y (2007) Acta Metall Sinica 43:11–16
36. Qiu C, Olson GB, Opalka SM, Anton DL (2004) J Phase Equilib Diff 25:520–527
37. Fromm E, Gebhardt E (1976) Gases and carbon in metals. Springer, Berlin
38. San-Martin A, Manchester FD (1987) Bull Alloy Phase Diagrams 8:431–437
39. Ide T, Iio Y, Nakajima H (2012) Metall Mater Trans A 43A:5140–5152
40. Ikeda T, Aoki T, Nakajima H (2005) Metall Mater Trans A36:77–86
41. Papp K, Csetenyi EK (1981) Scr Metall 15:161–164
42. Wright JH, Hocking MG (1972) Metall Trans 3:1749–1753
43. Kurz W, Fisher DJ (1998) Fundamental of solidification. Trans Tech Publications, Switzerland